

Assembly of PEG Microgels into Porous Cell-Instructive 3D Scaffolds via Thiol-Ene Click Chemistry

Shangjing Xin, Omar M. Wyman, and Daniel L. Alge*

The assembly of microgel building blocks into 3D scaffolds is an emerging strategy for tissue engineering. A key advantage is that the inherent microporosity of these scaffolds provides cells with a more permissive environment than conventional nanoporous hydrogels. Here, norbornene-bearing poly(ethylene glycol) (PEG) based microgels are assembled into 3D cell-instructive scaffolds using a PEG-dithiol linker and thiol-ene click photopolymerization. The bulk modulus of these materials depends primarily on the crosslink density of the microgel building blocks. However, the linker and initiator concentrations used during assembly have significant effects on cell spreading and proliferation when human mesenchymal stem cells (hMSCs) are incorporated in the scaffolds. The cell response is also affected by the properties of the modular microgel building blocks, as hMSCs growing in scaffolds assembled from stiff but not soft microgels activate Yes-associated protein signaling. These results indicate that PEG microgel scaffolds assembled via thiol-ene click chemistry can be engineered to provide a cell-instructive 3D milieu, making them a promising 3D platform for tissue engineering.

1. Introduction

Hydrogels are of broad interest for tissue engineering as their polymer networks can be engineered to mimic the native tissue environment.^[1] Synthetic hydrogels presenting tissue micro-environmental cues, such as bioactive molecules, topography, and substrate stiffness, have been proposed as scaffolds that recapitulate cell-instructive features of the natural extracellular matrix (ECM) for tissue engineering.^[2] However, an important and often overlooked challenge in developing 3D cell-instructive hydrogels is that conventional hydrogels are porous on the nanoscale and, therefore, constitute a restrictive barrier that must be degraded to permit cell spreading, migration, and deposition of a new ECM. Strategies using porogens, foaming agents, and freeze-drying have been developed to impart

microscale porosity in hydrogels for tissue engineering,^[3] but these methods generally require additives and postprocessing steps that may not be cytocompatible and can preclude cell incorporation during assembly.


An emerging paradigm in the development of porous hydrogels for tissue engineering is the assembly of 3D scaffolds from hydrogel microspheres or microgels.^[4] This approach involves synthesizing microgel building blocks in a preliminary step, packing them together, and then crosslinking them into a 3D structure. Due to the void spaces between the microspheres, this approach results in materials with a highly interconnected microporous structure without the need for any porogens or foaming agents. Griffin et al. reported that the interconnected microporosity of poly(ethylene glycol) (PEG) microgel based scaffolds

translates into accelerated healing compared to conventional hydrogels in a murine dermal wound healing model.^[4a] Similarly, Nih et al. recently demonstrated that hyaluronic acid microgel based scaffolds resulted in accelerated brain healing compared to conventional hydrogels when the materials were injected into stroke cavities in mice.^[5] In both studies, the superior results were attributed to the inherent microporosity of the microgel-based scaffolds permitting faster migration of endogenous cells into the scaffold. Other attractive features that make microgel-based scaffolds promising for tissue engineering are the ability to tune the physicochemical properties of the microgel building blocks to direct cell–material interactions and the potential for cell incorporation during microgel assembly, as recently demonstrated by Caldwell et al.^[4b]

While a number of chemical strategies are suitable for assembling microgels into 3D scaffolds, we have chosen to focus on thiol-ene chemistry because it offers several notable advantages. The first is that synthesizing suitable microgels is straightforward; microgels synthesized via an off-stoichiometric thiol-ene polymerization will be readily amenable to crosslinking with a bis-thiol or bis-norbornene linker, as appropriate. Thiol-ene synthesis of microgels also offers facile tuning of physicochemical properties by incorporating ECM mimetic peptides and modulating crosslink density.^[6] Specifically regarding assembly of microgels into 3D scaffolds, an important advantage of thiol-ene chemistry is its potential for spatiotemporal control via photoinitiation. In contrast, previously reported strategies such as transglutaminase mediated crosslinking, thiol-Michael

S. Xin, O. M. Wyman, Prof. D. L. Alge
Department of Biomedical Engineering
Texas A&M University
College Station, TX 77843, USA
E-mail: dalge@tamu.edu

Prof. D. L. Alge
Department of Materials Science and Engineering
Texas A&M University
College Station, TX 77843, USA

 The ORCID identification number(s) for the author(s) of this article can be found under <https://doi.org/10.1002/adhm.201800160>.

DOI: 10.1002/adhm.201800160

additions, and strain-promoted azide-alkyne crosslinking result in assembly upon mixing and do not afford spatiotemporal control.^[4a-c] Finally, thiol-ene chemistry offers fast reaction kinetics for assembly and superior cytocompatibility compared to chain-growth photopolymerization of vinyl groups,^[7] the latter of which is attractive for incorporating therapeutic cells like human mesenchymal stem cells (hMSCs) during assembly.

Here, we report the assembly of PEG microgel based scaffolds using photoinitiated thiol-norbornene click chemistry as a potential platform for hMSC delivery. The effects of varying concentrations of linker and initiator applied during assembly on mechanical properties and porosity of microgel scaffolds as well as hMSC cellularity were studied. The cell spreading trends with scaffold stiffness were also compared between hMSCs seeded in conventional bulk hydrogels and microgel scaffolds. Finally, Yes-associated protein (YAP) nuclear localization in hMSCs cultured in microgel scaffolds was studied to evaluate cell mechanosensing in scaffolds prepared from microgels with different moduli.

2. Results

2.1. Assembly of PEG Microgels into Porous Scaffolds with Thiol-Ene Chemistry

In order to assemble scaffolds, norbornene bearing PEG microgels were packed in an 8 mm diameter silicone circular mold with the addition of PEG-dithiol (DT) linker and lithium acylphosphinate (LAP) photoinitiator and then the samples were

exposed to UV light for polymerization (365 nm, 10 mW cm⁻², 3 min; **Figure 1a**). The microgels generated from a set of controlled electrospaying parameters were ≈200 μm in diameter, as characterized by microscopy (Figure S2, Supporting Information). **Figure 1b** shows a macroscopic image of a thiol-ene PEG5 scaffold, and the particulate morphology of the surface is clearly visible. Confocal microscopy imaging of AF488-labeled scaffolds revealed interconnected pores that were several hundred micrometers in size (**Figure 1c**). To further characterize the assembly process, the storage moduli of PEG5 and PEG20 scaffolds were monitored during in situ photopolymerization of microgels on a rheometer (**Figure 1d**). Upon irradiation, a 1.5–2-fold increase in storage modulus was observed within 10 s and the final modulus of the PEG5 scaffolds was higher than that of the PEG20 scaffolds. Fluorophore-labeled dextran was also diffused into the microgel scaffolds and demonstrated the interconnectivity of the micropore structure (**Figure 1e**). In addition, photomasks with simple shapes were applied during UV irradiation to emphasize the spatiotemporal control of thiol-ene microgel assembly (**Figure S3**, Supporting Information).

2.2. Characterization of Scaffold Properties

During the assembly process, varying amounts of linker and initiator were applied and their effects on bulk mechanical properties and porosity were studied (**Figure 2**). As the [SH]:[ene] ratio of PEG5 microgels was 0.75:1, the theoretical concentration of available norbornene groups was 18×10^{-3} M for PEG5. While this translates into an upper boundary of 9×10^{-3} M for PEG-DT

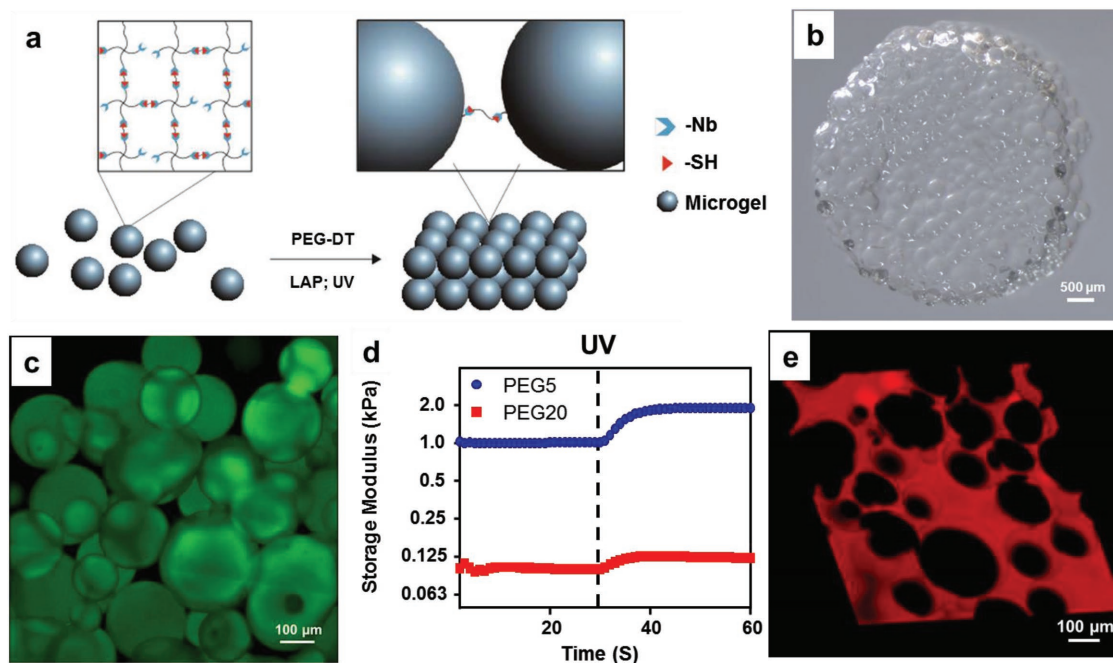


Figure 1. PEG microgel scaffolds with interconnected micropores are successfully assembled through thiol-ene photopolymerization. a) Schematic illustrating thiol-ene assembly of microgels into scaffolds. b) Stereomicroscope image of a PEG5 microgel scaffold. c) Z-stack image of a PEG5 microgel scaffold labeled with Alexa Fluor 488-succinimidyl ester (top-down view of a 3D reconstruction). d) Storage modulus evolution of PEG5 and PEG20 during in situ photopolymerization into scaffolds. e) Representative 3D image of a microgel scaffold immersed in solution of fluorescently labeled high molecular weight dextran, demonstrating pore interconnectivity.

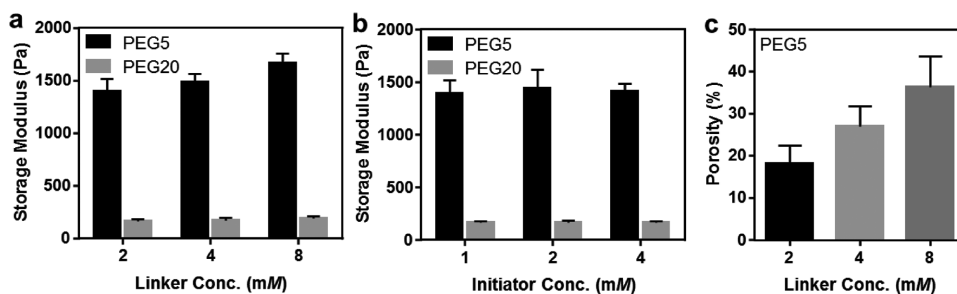


Figure 2. Effect of varying linker and initiator concentrations on scaffold properties. Storage modulus of PEG5 scaffolds assembled using a) varying linker and 1×10^{-3} M initiator and b) 2×10^{-3} M linker and varying initiator concentrations. c) Porosity of PEG5 scaffolds prepared with the varying linker concentrations and 1×10^{-3} M initiator. Data are for $n = 3$ scaffolds for each group.

to react with all available norbornene groups, we found that only 2×10^{-3} M PEG-DT was required to assemble PEG5 microgels into bulk scaffolds, as shown in Figure 2a. Interestingly, adding more PEG-DT only slightly enhanced the storage modulus of microgel scaffolds for both PEG5 and PEG20. Similarly, varying the amount of LAP did not influence the storage modulus significantly (Figure 2b). However, increasing the amount of PEG-DT linker did increase the scaffold porosity from 17% to 36% (Figure 2c), presumably due to the different volumes of PEG-DT solution added. As shown in fluorescent z-stack images (Figure S4, Supporting Information), microgels were distributed evenly throughout the scaffolds in the low linker concentration group, while large voids and clusters of microgels were observed in the high linker concentration group.

2.3. Characterization of hMSC Viability, Spreading, and Proliferation

Following characterization of microgel scaffolds, hMSCs were encapsulated within PEG5 scaffolds with varying amounts of linker and initiator. As shown in Video S1 (Supporting

Information), hMSCs spread to surround the microgels and grew within the micropores after 24 h of culture to form a 3D cellular network within the microgel scaffolds. However, drastic differences in cell numbers and spreading were observed for the varying concentrations of linker and initiator (Figure 3a). Despite the lower scaffold porosity, cellularity was enhanced in the low concentration groups, and the cell volume was two to threefold higher compared to the high concentration groups (Figure 3b). These results were not due to viability differences, as Live/Dead staining indicated high viability (>80%) in all groups (Figure 3c and Figure S5, Supporting Information). Further analysis showed that 36% of hMSCs encapsulated within microgel scaffolds in the low concentration group were proliferating, compared to only 7% with a high PEG-DT concentration and 2% with a high LAP concentration (Figure 3d and Figure S6, Supporting Information).

2.4. Effect of Microporosity on hMSC Spreading Trends with Increasing Stiffness

hMSC spreading trends in conventional bulk hydrogels and microgel scaffolds were also compared (Figure 4). Prior to

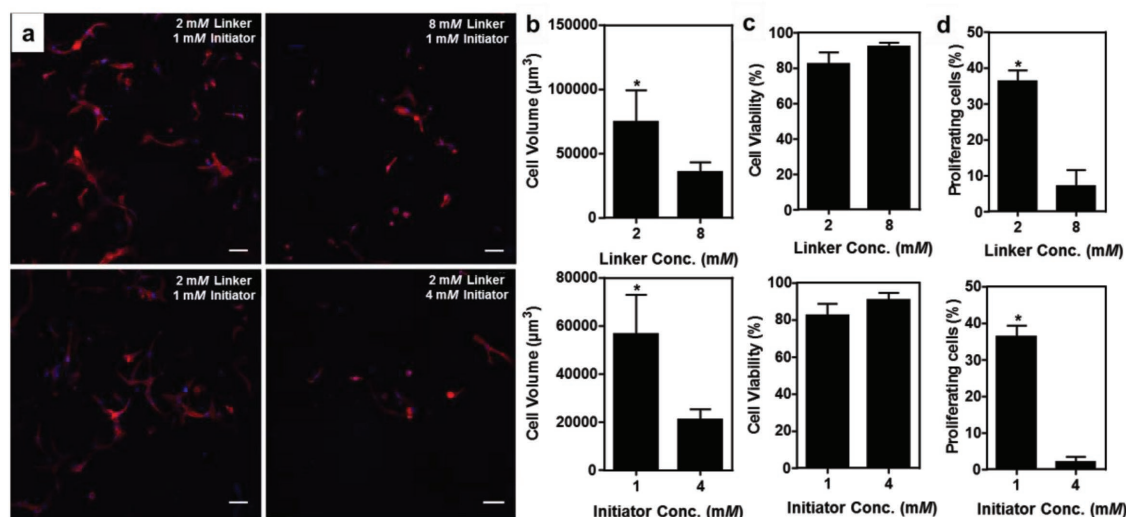


Figure 3. hMSC spreading and proliferation in microgel scaffolds was influenced by the linker and initiator concentrations used during scaffold assembly. a) Maximum intensity Z-projection of cytoskeleton staining of hMSCs cultured in PEG5 scaffolds after 1 d. Red represents F-actin and blue represents nuclei. Scale bars are 100 µm. b) Cell volume, c) cell viability, and d) percent proliferating cells plotted versus linker and initiator concentrations after 1 d. Data are for $n > 50$ cells. $*p < 0.001$.

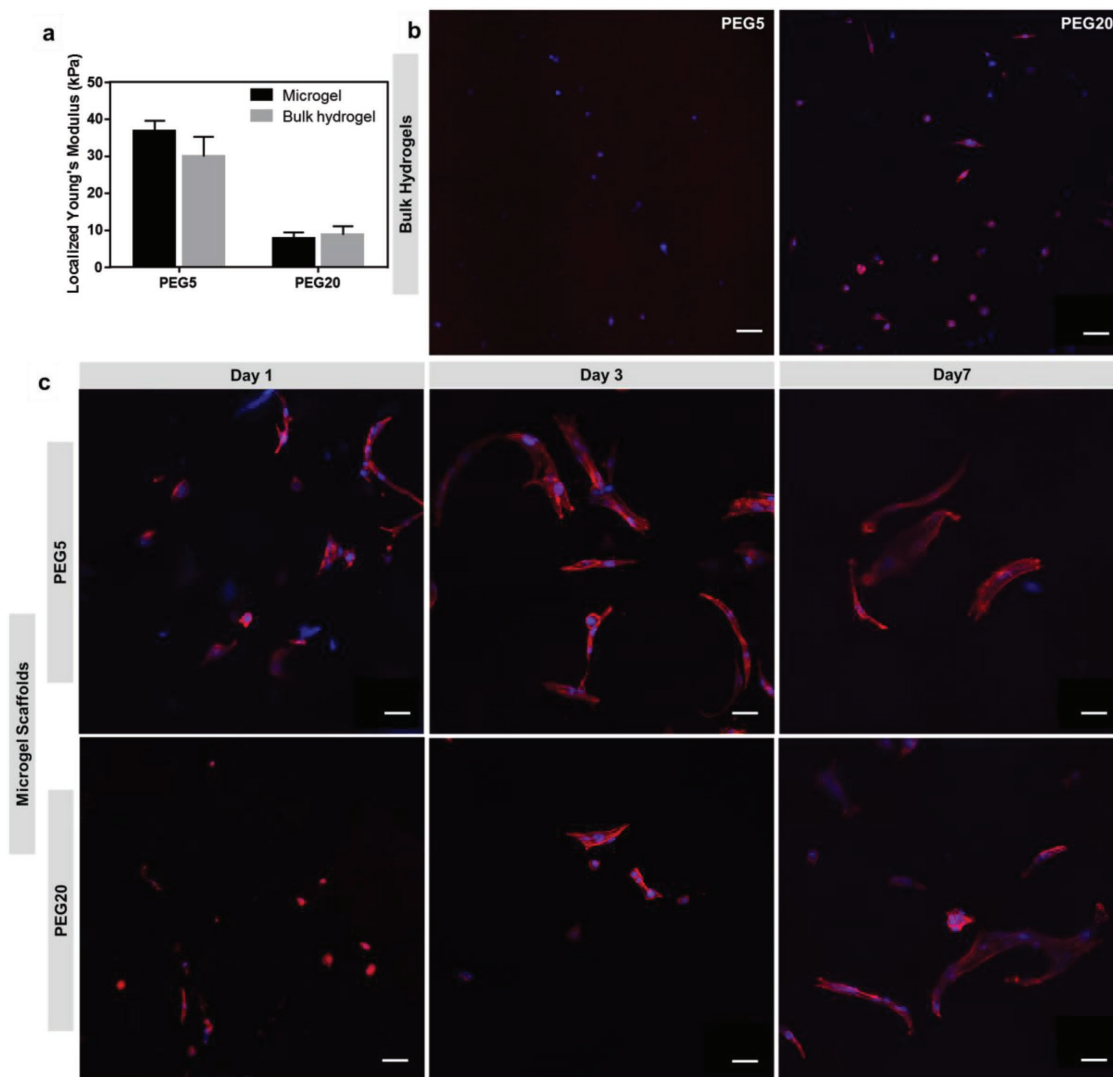


Figure 4. hMSCs in microgel scaffolds of varying stiffness exhibit opposite trends in spreading compared to conventional hydrogels. a) Localized Young's modulus of individual microgels and bulk hydrogels made from PEG5 and PEG20 measured by AFM. b) Maximum intensity Z-projection of cytoskeleton staining of hMSCs cultured in PEG5 and PEG20 bulk hydrogels after 1 d. c) Maximum intensity Z-projection of cytoskeleton staining of hMSCs cultured in PEG5 and PEG20 microgel scaffolds after 1, 3, and 7 d. Red represents F-actin and blue represents nuclei. Scale bars are 50 μ m.

incorporating hMSCs, we compared the moduli of the microgels and conventional hydrogels. Nanoindentation testing by atomic force microscopy (AFM) on individual microgels revealed localized Young's moduli of 35.8 and 7.6 kPa for PEG5 and PEG20 microgels, respectively (Figure 4a). Bulk hydrogels from the same molecular weight PEG-norbornene (Nb) exhibited equivalent localized moduli. In bulk hydrogels, hMSCs spread better in PEG20 than PEG5 after 24 h (Figure 4b), as expected due to the lower crosslinking density. However, the degree of cell spreading was inferior to the microgel scaffolds. When cultured in microgel scaffolds, hMSCs spread well along the surface of the PEG5 spheres and exhibited large cell volume after 24 h, whereas they stayed rounded within PEG20 scaffolds (Figure 4c). As the culture extended, hMSCs continued to proliferate and spread in both groups at day 7.

2.5. Effect of Microgel Mechanical Properties on YAP Nuclear Localization

In order to study the effects of microgel stiffness on the cell response, we immunostained for YAP after 72 h culture to evaluate hMSC mechanosensing in the microgel scaffolds. Fluorescence images from confocal microscopy indicated enhanced YAP nuclear localization in microgel scaffolds with increasing stiffness. Quantification of the YAP nuclear/cytosolic ratio revealed that the YAP relative nuclear intensity was approximately twofold higher for hMSCs cultured in PEG5 scaffolds than in PEG20 scaffolds (Figure 5a). The averaged cell volume in PEG5 scaffolds was also eightfold higher (Figure 5b). Some cells in PEG20 scaffolds appeared to aggregate with other cells as shown in representative images (Figure 5c).

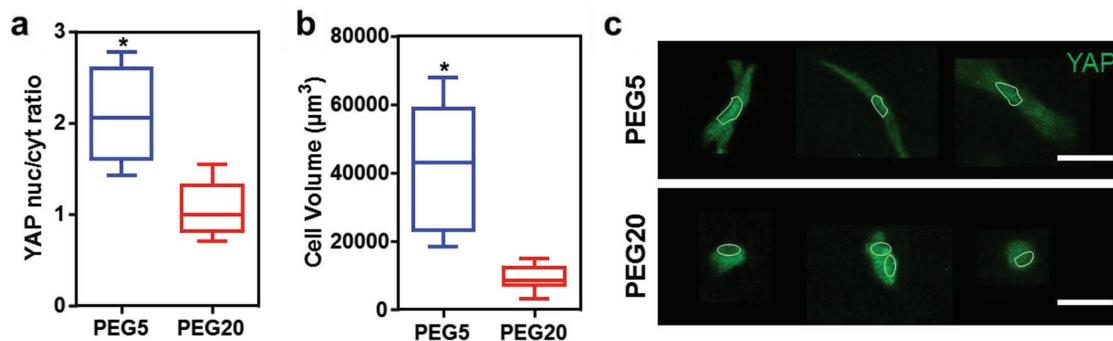


Figure 5. YAP nuclear activation in hMSCs is upregulated by increasing matrix stiffness in microgel scaffolds. a) YAP/TAZ nuclear localization for hMSCs encapsulated within PEG5 and PEG20 microgel scaffolds. b) Average cell volume of hMSCs cultured in microgel scaffolds of varying stiffness. c) Representative images of hMSC YAP nuclear localization. White circles represent the position of nucleus (Note: two cells are shown clustered together in the middle image for the PEG 20 group). Scale bars are 50 μm . $*p < 0.001$.

3. Discussion

The assembly of microgels into 3D microporous hydrogels is an emerging paradigm in biomaterials. Because of their interconnected microporosity, microgel-based scaffolds may be more effective for certain tissue engineering applications than conventional hydrogels, which are only nanoporous.^[4a,b] These scaffolds are more permissive to cell spreading and migration, and tuning the physicochemical properties of the microgels should provide a means for directing the cellular response. However, cell–material interactions are different in these materials compared to conventional hydrogels, and the effects of variables in the microgel scaffold design and assembly processes on cells have not been studied. The objective of this work was to address this knowledge gap.

Here, we used thiol-ene click chemistry to electro-spray PEG microgel and assemble them into scaffolds. This approach has some important advantages, including facile incorporation of bioactive peptide precursors and rapid kinetics.^[8] We used norbornenes to conjugate thiolated Arg-Gly-Asp (RGD) cell adhesive peptides and assemble the microgels via a PEG-DT linker, although any bis-thiol linker could be used. Importantly, we were also able to tune the crosslinking density and modulus of the microgel building blocks by adjusting the molecular weight of the PEG-Nb macromer. These microgel building blocks were rapidly assembled into 3D scaffolds upon UV irradiation, which is helpful to shorten cell encapsulation time (Figure 1d). In addition, we observed interconnected micropores within the scaffolds, which indicates the success of synthesizing microporous scaffolds using this method (Figure 1e).

We also seeded hMSCs into the scaffolds during microgel assembly. Our results complement the recent work of Caldwell et al. who showed that hMSC spreading differs depending on microgel size,^[4b] but did not study how the extent of crosslinking between the microgels affects the cells. To understand this latter variable, we studied hMSC spreading when using varying amounts of linker and initiator for microgel assembly. While increasing the amount of linker resulted in increased porosity and looser packing of the microgels, likely due to the larger volume of solution being added, this was not beneficial to the cell response. Rather, our results show that low concentrations of linker and initiator are critical for

cell spreading and growth in our system (Figure 3). As shown in Figure S4 (Supporting Information), microgels tended to fuse together in the high linker concentration group, which appeared to limit the ability of cells to spread. It is also possible that the use of a PEG-based linker may have reduced the availability of RGD peptides, which would also inhibit cell spreading. Regardless, in our present system, using low concentrations of linker and initiator for microgel assembly appears to be critical.

Within microgel-based scaffolds, cells interact with the microgel surfaces as if they were a 2D material. This feature is significant because recent studies have noted differences in cell–material interactions between 2D and 3D environments.^[9] Because of the restrictive environment in conventional bulk hydrogels, cells spread less in more densely crosslinked networks and degradation is required to allow more spreading.^[10] Indeed, we observed this trend in hMSC spreading in conventional PEG thiol-ene hydrogels even with a peptide degradable crosslinker (Figure 4b). In contrast, when culturing in nondegradable microgel scaffolds prepared with the same PEG molecular weight and thiol:ene ratio, and thus the same crosslinking density, the spreading trend of hMSCs with stiffness in the 3D environment was similar to what is observed in 2D cultures (Figure 4c). This observation confirmed that the microporosity of microgel scaffolds provides cells with a 3D environment that is more permissive to cell spreading.

Inspired by the fact that our cell spreading trends were similar to 2D cultures, we subsequently investigated hMSC mechanosensing in our microgel scaffolds to see if this would also be similar. We specifically characterized YAP/ transcriptional coactivator with PDZ-binding motif (TAZ) nuclear staining in scaffolds assembled from microgels of varying moduli, since modulus is well known to influence hMSC fate and function^[11] and YAP/TAZ is a well-established marker of mechanosensing.^[12] Importantly, Caliri et al. recently reported that hMSC mechanosensing in conventional hydrogels is distinctly different from 2D cultures, with higher modulus hydrogels resulting in decreased rather than increased YAP nuclear staining.^[13] In contrast, we observed the opposite trend in our microgel scaffolds, as hMSCs exhibited a higher YAP nuclear/cytoplasmic localization and larger cell volume in scaffolds assembled from higher modulus microgels (35.8 kPa vs 7.6 kPa; Figure 5). Based on this result, hMSC mechanosensing in microgel

scaffolds appears to be similar to what has been observed in 2D culture,^[14] which could be promising for the future development of 3D cell-instructive scaffolds for tissue engineering.

4. Conclusion

We demonstrate here thiol-ene chemistry based assembly of porous PEG microgel scaffolds. In addition, we show the suitability of these materials as a platform for hMSC encapsulation. Key findings are that low concentrations of crosslinker and initiator applied during the assembly process are critical for maintaining a permissive environment within these scaffolds, and that the PEG microgel properties can be tuned to influence the behavior of cells incorporated during assembly. The 3D permissive environment due to microporosity provides a means to regulate cell spreading and mechanosensing by material properties, with trends in cell behavior being similar to what has been observed in 2D cultures. Based on these results, these materials appear to be a promising platform that could have broad utility for tissue engineering and regenerative medicine. Future studies should investigate whether microgels containing specific biophysical and biochemical cues can be used to enhance *in vivo* tissue engineering efficacy.

5. Experimental Section

Materials: Tetrafunctional PEG-Nb macromers (5 and 20 kDa) were synthesized from PEG-hydroxyl precursors via esterification with 5-norbornene-2-carboxylic acid (Alfa Aesar) using diisopropyl carbodiimide activation, as described by Jivan et al.^[15] The polymers were dialyzed against deionized water prior to use, and percent functionalization was determined to be greater than 95% via ¹H NMR spectroscopy analysis. The cell adhesive peptide CGRGDS was prepared via microwave-assisted solid phase peptide synthesis and standard Fmoc methods. The coupling times and temperatures were 6 min at 50 °C for cysteine and 5 min at 75 °C for other amino acids. Amino acids were activated with *N,N,N',N'*-tetramethyl-O-(1H-benzotriazol-1-yl)uronium hexafluorophosphate (Chem-Impex), and Fmoc deprotection was performed with 5% piperazine (Alfa Aesar) and 0.1 M hydroxybenzotriazole (Advanced Chemtech) for 3 min at 75 °C. Peptides were cleaved from the resin with a cocktail of trifluoroacetic acid (TFA, Sigma)–triisopropyl silane (Sigma)–water–phenol (Sigma) (94:2.5:2.5:1), precipitated in ice cold diethyl ether, and then purified by reverse-phase high performance liquid chromatography (HPLC) in water/acetonitrile with 0.1% TFA. Peptide composition was verified by matrix-assisted laser desorption/ionization time of flight mass spectrometry (MALDI-TOF MS) analysis. LAP was synthesized following the methods of Fairbanks et al. without modification and verified by ¹H NMR spectroscopy and electrospray ionization (ESI) MS prior to use^[8a].

Preparation of Electrosprayed Microgels: Tetra-arm PEG-Nb and PEG-DT ($M_w = 3400$ Da, Laysan Bio.) were mixed off-stoichiometrically with cell-adhesive peptide ligand CGRGDS (1×10^{-3} M) and LAP (2×10^{-3} M). The final working concentration of PEG-Nb was 10 wt% and the [SH]:[ene] ratio for PEG-DT and PEG-Nb was 0.75:1 so that unreacted norbornene groups would be available for microgel assembly. Two PEG-Nb molecular weights (5 and 20 kDa) were used to prepare microgels with varying crosslink density and mechanical properties (termed PEG5 and PEG20, respectively). The precursor solutions were then electrosprayed into light mineral oil with Span 80 (0.5 wt%), similar to the approach of Qayyum et al.^[16]

The submerged electrospraying setup consisted of a DC voltage source (ES30N-5W, Gamma High Voltage Research), a syringe pump (KDS 100, KD Scientific), a syringe with a blunt needle, a grounded ring, a UV light source, and light mineral oil for microgel collection

(Figure S1, Supporting Information). The voltage was adjusted to accommodate for the slightly different viscosities of the microgel precursor solutions with different molecular weight PEG-Nb. Here, 4 and 6 kV were applied for PEG5 and PEG20 microgel synthesis, respectively. Other parameters included 12 mL h⁻¹ flow rate, 16 mm needle-to-ring distance, and 22 gauge needle size. The mineral oil was irradiated with 365 nm UV light (60 mW cm⁻², Lumen Dynamics Omnicure S2000 Series) during electrospraying to photopolymerize the microgels. The resulting microgels were centrifuged, washed one time with 30% ethanol, and then washed five times with phosphate buffered saline to remove mineral oil and surfactant. The microgels were swollen at 4 °C overnight to reach equilibrium before use.

Preparation of 3D Scaffolds: To prepare thiol-ene PEG microgel scaffolds, microgels were filled in an 8 mm diameter, 50 μL silicone circular mold. Subsequently, varying volumes of 20 wt% PEG-DT (2, 4, or 8 μL) and 100×10^{-3} M LAP (1, 2, or 4 μL) were added to achieve the desired concentrations and mixed by pipetting. The microgels were then assembled into scaffolds by UV irradiation (365 nm, 10 mW cm⁻², 3 min). This assembly process was also monitored by *in situ* photopolymerization on a rheometer (Physica MCR 301, Anton Paar) under a time sweep at 1% strain and 1 rad s⁻¹.

For Comparison in Cell Studies: Bulk hydrogels were prepared using tetra-arm PEG-Nb (5 and 20 kDa, 10 wt%) and enzymatically degradable peptide crosslinker KCGPQGIWGQCK (purchased from GL Biochem) with cell-adhesive peptide ligand CGRGDS (1×10^{-3} M) and LAP (2×10^{-3} M). The [SH]:[ene] ratio on bulk hydrogels was also maintained at 0.75:1. An amount of 50 μL of precursor solution was added into an 8 mm silicone circular mold and photo-crosslinked by UV irradiation (365 nm, 10 mW cm⁻², 3 min).

Characterization: The macroscopic morphology of microgel scaffolds was observed using a stereomicroscope (Stemi 508, Zeiss) with 1X objective. The inner structure of microgel scaffolds was imaged by confocal microscopy (FV1000, Olympus). For visualization, Alexa Fluor 488-succinimidyl ester (Invitrogen) was conjugated to the N-terminus of the CGRGDS peptide in the microgels. Forty z-slices were taken in each z-stack, spanning a total of 200 μm depth. To visualize the interconnected pore structure, high molecular weight tetramethylrhodamine isothiocyanate-dextran (155 kDa, Sigma) was diffused into microgel scaffolds and imaged by confocal microscopy.

In Addition: The macroscopic mechanical properties of microgel scaffolds with varying linker and initiator concentrations were measured by oscillatory shear rheology (Physica MCR 301, Anton Paar) at 1% strain and 1 rad s⁻¹ with a gap size of 600 μm. Microgels were also sectioned into 25 μm slices on a cryostat, and the localized Young's modulus of individual microgels and bulk hydrogels were measured by AFM (Dimension Icon, Bruker) with a SiO₂ colloidal probe (5 μm diameter, spring constants 0.6 N m⁻¹; Novascan).^[17]

Cell Culture: hMSCs were obtained from the Institute of Regenerative Medicine at Texas A&M University and cultured in low-glucose Dulbecco's Modified Eagle's Medium (Corning) with 10% v/v fetal bovine serum, penicillin (50 U mL⁻¹), streptomycin (50 μg mL⁻¹), and basic fibroblast growth factor (1 ng mL⁻¹) at 5% CO₂ and 37 °C. hMSCs were used up to passage 5. Single-cell suspensions of hMSCs (10 μL) were mixed with microgels in the silicone mold during the assembly process for cell seeding at a density of 20 000 cells per scaffold. To seed hMSCs into bulk hydrogels, cell suspensions were mixed with precursor solutions and encapsulated via UV crosslinking (365 nm, 10 mW cm⁻², 3 min).

Immunostaining and Imaging: The viability of hMSCs encapsulated in microgel scaffolds was tested using Live/Dead viability kit (L3224, Invitrogen). For immunostaining, samples were fixed after the desired culture time using 4% formaldehyde for 15 min at room temperature. Cytoskeletal staining was performed using rhodamine phalloidin (1:40, Invitrogen), and cell nuclei were stained with 4',6-diamidino-2-phenylindole (DAPI) (1:1000, Biolegend). hMSC proliferation after 24 h was evaluated using the Click-iT Edu Alexa Fluor 647 kit (C10340, Invitrogen). Evaluation of cell mechanotransduction was performed by immunohistochemistry utilizing antibodies against YAP (1:200, Santa Cruz). Goat anti-mouse

IgG-FITC (1:100, Jackson ImmunoResearch) was used as a fluorescent secondary antibody. Microgel scaffolds were then counter stained with DAPI (1:1000, Biolegend). All the samples were imaged in a glass bottom petri dish (MarTek) by confocal microscopy (FV1000, Olympus).

Image Analysis: All image analysis was performed using ImageJ software (NIH). For porosity measurements, each z-stack of fluorescent-labeled microgel scaffolds was thresholded to differentiate between the scaffold and pores. The black voxels were then measured using Image J's Voxel Counter plugin to obtain the thresholded volume and volume of stack. The porosity of scaffolds was then calculated as shown in the formula below

$$\text{Porosity(\%)} = \frac{\text{Thresholded volume}}{\text{Volume of stack}} * 100\% \quad (1)$$

For cell volume quantification, each cellular domain was determined by an intensity-based thresholding method from actin staining in z-stack images. The volume of each cell was measured by Image J's 3D Objects Counter plugin. YAP nuclear/cytosolic ratio was calculated by the ratio of average intensity in nucleus and cytosol. Volume and intensity were also determined by Image J's 3D Objects Counter plugin and the formula shown below

$$\text{YAP nuclear/cytosolic ratio} = \frac{\frac{\text{Nuclear YAP intensity}}{\text{Volume of nucleus}}}{\frac{\text{Cytosolic YAP intensity}}{\text{Volume of cytosol}}} \quad (2)$$

Statistical Analysis: All experiments were conducted with at least three independent scaffolds, and four different regions per scaffold were imaged. Cellular quantification was measured with at least 50 cells per group. Results are reported as the mean \pm standard deviation. Student's *t*-test was used to determine significant differences between two groups. Significance is indicated by * corresponding to $p < 0.001$, respectively.

Supporting Information

Supporting Information is available from the Wiley Online Library or from the author.

Acknowledgements

The authors would like to thank Dr. Wilson Serem at the Materials Characterization Facility of TAMU for assistance with AFM testing. This research was supported by the National Institutes of Health (R21 AR071625-01 to D.L.A.) and Texas A&M Engineering Experiment Station (start-up funds to D.L.A.). The Supporting Information for the article was replaced on June 6, 2018 after initial online publication.

Conflict of Interest

The authors declare no conflict of interest.

Keywords

cell instructive, mesenchymal stem cells, microgel, PEG, thiol-ene

Received: February 12, 2018
Published online: April 16, 2018

- [1] a) Y. Jiang, J. Chen, C. Deng, E. J. Suuronen, Z. Zhong, *Biomaterials* **2014**, *35*, 4969; b) D. L. Alge, M. A. Azagarsamy, D. F. Donohue, K. S. Anseth, *Biomacromolecules* **2013**, *14*, 949.
- [2] a) R. Cruz-Acuña, A. J. García, *Matrix Biol.* **2017**, *57*, 324; b) X. Zhao, Q. Lang, L. Yildirimer, Z. Y. Lin, W. Cui, N. Annabi, K. W. Ng, M. R. Dokmeci, A. M. Ghaemmaghami, A. Khademhosseini, *Adv. Healthcare Mater.* **2016**, *5*, 108; c) M. F. Cutiongco, S. H. Goh, R. Aid-Launais, C. Le Visage, H. Y. Low, E. K. Yim, *Biomaterials* **2016**, *84*, 184.
- [3] a) N. Annabi, J. W. Nichol, X. Zhong, C. Ji, S. Koshy, A. Khademhosseini, F. Dehghani, *Tissue Eng., Part B* **2010**, *16*, 373; b) Y. Xu, H. Wang, C. Luan, F. Fu, B. Chen, H. Liu, Y. Zhao, *Adv. Funct. Mater.* **2018**, *28*, 1704458; c) N. Huebsch, E. Lippens, K. Lee, M. Mehta, S. T. Koshy, M. C. Darnell, R. M. Desai, C. M. Madl, M. Xu, X. Zhao, *Nat. Mater.* **2015**, *14*, 1269; d) A. Borisova, M. De Bruyn, V. L. Budarin, P. S. Shuttleworth, J. R. Dodson, M. L. Segatto, J. H. Clark, *Macromol. Rapid Commun.* **2015**, *36*, 774.
- [4] a) D. R. Griffin, W. M. Weaver, P. O. Scumpia, D. Di Carlo, T. Segura, *Nat. Mater.* **2015**, *14*, 737; b) A. S. Caldwell, G. T. Campbell, K. M. Shekero, K. S. Anseth, *Adv. Healthcare Mater.* **2017**, *6*, 1700254; c) E. Sideris, D. R. Griffin, Y. Ding, S. Li, W. M. Weaver, D. Di Carlo, T. Hsiai, T. Segura, *ACS Biomater. Sci. Eng.* **2016**, *2*, 2034; d) W. Zhou, J. M. Stukel, H. L. Cebull, R. K. Willits, *Macromol. Biosci.* **2016**, *16*, 535; e) E. A. Scott, M. D. Nichols, R. Kuntz-Willits, D. L. Elbert, *Acta Biomater.* **2010**, *6*, 29; f) K. J. France, F. Xu, T. Hoare, *Adv. Healthcare Mater.* **2018**, *7*, 1700927.
- [5] L. R. Nih, E. Sideris, S. T. Carmichael, T. Segura, *Adv. Mater.* **2017**, *29*, 1606471.
- [6] B. D. Fairbanks, M. P. Schwartz, A. E. Halevi, C. R. Nuttelman, C. N. Bowman, K. S. Anseth, *Adv. Mater.* **2009**, *21*, 5005.
- [7] a) C.-C. Lin, A. Raza, H. Shih, *Biomaterials* **2011**, *32*, 9685; b) A. D. Shubin, T. J. Felong, D. Graunke, C. E. Ovitt, D. S. Benoit, *Tissue Eng., Part A* **2015**, *21*, 1733.
- [8] a) B. D. Fairbanks, M. P. Schwartz, C. N. Bowman, K. S. Anseth, *Biomaterials* **2009**, *30*, 6702; b) C. M. Magin, D. L. Alge, K. S. Anseth, *Biomed. Mater.* **2016**, *11*, 022001; c) J. D. McCall, K. S. Anseth, *Biomacromolecules* **2012**, *13*, 2410.
- [9] a) P. Worthington, D. J. Pochan, S. A. Langhans, *Front. Oncol.* **2015**, *5*, 92; b) D. Thomas, T. O'Brien, A. Pandit, *Adv. Mater.* **2018**, *30*, 1703948; c) Y. Li, Y. Xiao, C. Liu, *Chem. Rev.* **2017**, *117*, 4376.
- [10] a) S. K. Seidlits, Z. Z. Khaing, R. R. Petersen, J. D. Nickels, J. E. Vanscoy, J. B. Shear, C. E. Schmidt, *Biomaterials* **2010**, *31*, 3930; b) S. Khetan, M. Guvendiren, W. R. Legant, D. M. Cohen, C. S. Chen, J. A. Burdick, *Nat. Mater.* **2013**, *12*, 458.
- [11] a) A. J. Engler, S. Sen, H. L. Sweeney, D. E. Discher, *Cell* **2006**, *126*, 677; b) J. H. Wen, L. G. Vincent, A. Fuhrmann, Y. S. Choi, K. C. Hribar, H. Taylor-Weiner, S. Chen, A. J. Engler, *Nat. Mater.* **2014**, *13*, 979.
- [12] a) S. Dupont, L. Morsut, M. Aragona, E. Enzo, S. Giullitti, M. Cordenonsi, F. Zanconato, J. Le Digabel, M. Forcato, S. Bicciato, *Nature* **2011**, *474*, 179; b) C. Yang, M. W. Tibbitt, L. Basta, K. S. Anseth, *Nat. Mater.* **2014**, *13*, 645.
- [13] S. R. Caliri, S. L. Vega, M. Kwon, E. M. Soulas, J. A. Burdick, *Biomaterials* **2016**, *103*, 314.
- [14] W. J. Hadden, J. L. Young, A. W. Holle, M. L. McFetridge, D. Y. Kim, P. Wijesinghe, H. Taylor-Weiner, J. H. Wen, A. R. Lee, K. Bieback, *Proc. Natl. Acad. Sci. USA* **2017**, *114*, 5647.
- [15] F. Jivan, R. Yegappan, H. Pearce, J. K. Carrow, M. J. McShane, A. K. Gaharwar, D. L. Alge, *Biomacromolecules* **2016**, *17*, 3516.
- [16] A. S. Qayyum, E. Jain, G. Kolar, Y. Kim, S. A. Sell, S. P. Zustiak, *Biofabrication* **2017**, *9*, 025019.
- [17] P. B. Welzel, J. Friedrichs, M. Grimmer, S. Vogler, U. Freudenberg, C. Werner, *Adv. Healthcare Mater.* **2014**, *3*, 1849.